Cascade-coupled racetrack resonators based on the Vernier effect in the mid-infrared

Benedetto Troia,[1,*] Ali Z. Khokhar,[2] Milos Nedeljkovic,[2] Jordi Soler Penades,[2] Vittorio M. N. Passaro,[1] and Goran Z. Mashanovich[2]

[1]*Department of Electrical and Information Engineering, Politecnico di Bari, Via E. Orabona 4, 70125 Bari, Italy*
[2]*Optoelectronics Research Centre, University of Southampton, Southampton SO17 1BJ, UK*
[*]*benedetto.troia@poliba.it*

Abstract: In this paper we report the experimental demonstration of racetrack resonators in silicon-on-insulator technology platform operating in the mid-infrared wavelength range of 3.7-3.8 μm. Insertion loss lower than 1 dB and extinction ratio up to 30 dB were measured for single resonators. The experimental characterization of directional couplers and bending losses in silicon rib waveguides are also reported. Furthermore, we present the design and fabrication of cascade-coupled racetrack resonators based on the Vernier effect. Experimental spectra of Vernier architectures were demonstrated for the first time in the mid-infrared with insertion loss lower than 1 dB and maximum interstitial peak suppression of 10 dB.

OCIS codes: (040.6040) Silicon; (230.4555) Coupled resonators; (130.3120) Integrated optics devices.

References and links

1. R. Soref, "Mid-infrared photonics in silicon and germanium," Nat. Photonics **4**(8), 495–497 (2010).
2. C. Y. Wang, T. Herr, P. Del'Haye, A. Schliesser, J. Hofer, R. Holzwarth, T. W. Hänsch, N. Picqué, and T. J. Kippenberg, "Mid-infrared optical frequency combs at 2.5 μm based on crystalline microresonators," Nat. Commun. **4**(1354), 1–7 (2013).
3. G. Z. Mashanovich, M. M. Milošević, M. Nedeljkovic, N. Owens, B. Xiong, E. J. Teo, and Y. Hu, "Low loss silicon waveguides for the mid-infrared," Opt. Express **19**(8), 7112–7119 (2011).
4. M. M. Milošević, M. Nedeljkovic, T. M. Ben Masaud, E. Jaberansary, H. M. H. Chong, N. G. Emerson, G. T. Reed, and G. Z. Mashanovich, "Silicon waveguides and devices for the mid-infrared," Appl. Phys. Lett. **101**(12), 121105 (2012).
5. C. Reimer, M. Nedeljkovic, D. J. M. Stothard, M. O. S. Esnault, C. Reardon, L. O'Faolain, M. Dunn, G. Z. Mashanovich, and T. F. Krauss, "Mid-infrared photonic crystal waveguides in silicon," Opt. Express **20**(28), 29361–29368 (2012).
6. M. Nedeljkovic, A. Z. Khokhar, Y. Hu, X. Chen, J. Soler Penades, S. Stankovic, H. M. H. Chong, D. J. Thomson, F. Y. Gardes, G. T. Reed, and G. Z. Mashanovich, "Silicon photonic devices and platforms for the mid-infrared," Opt. Mater. Express **3**(9), 1205–1214 (2013).
7. M. Nedeljkovic, S. Stanković, C. J. Mitchell, A. Z. Khokhar, S. A. Reynolds, D. J. Thomson, F. Y. Gardes, C. G. Littlejohns, G. T. Reed, and G. Z. Mashanovich, "Mid-infrared thermo-optic modulators in SOI," IEEE Photon. Technol. Lett. **26**(13), 1352–1355 (2014).
8. D. J. Thomson, L. Shen, J. J. Ackert, E. Huante-Ceron, A. P. Knights, M. Nedeljkovic, A. C. Peacock, and G. Z. Mashanovich, "Optical detection and modulation at 2μm-2.5μm in silicon," Opt. Express **22**(9), 10825–10830 (2014).
9. M. Muneeb, X. Chen, P. Verheyen, G. Lepage, S. Pathak, E. Ryckeboer, A. Malik, B. Kuyken, M. Nedeljkovic, J. Van Campenhout, G. Z. Mashanovich, and G. Roelkens, "Demonstration of Silicon-on-insulator mid-infrared spectrometers operating at 3.8 μm," Opt. Express **21**(10), 11659–11669 (2013).
10. Y. Hu, T. Li, D. J. Thomson, X. Chen, J. S. Penades, A. Z. Khokhar, C. J. Mitchell, G. T. Reed, and G. Z. Mashanovich, "Mid-infrared wavelength division (de)multiplexer using an interleaved angled multimode interferometer on the silicon-on-insulator platform," Opt. Lett. **39**(6), 1406–1409 (2014).
11. Z. Cheng, X. Chen, C. Y. Wong, K. Xu, and H. K. Tsang, "Mid-infrared suspended membrane waveguide and ring resonator on silicon-on-insulator," IEEE Photon. J. **4**(5), 1510–1519 (2012).
12. Y. Xia, C. Qiu, X. Zhang, W. Gao, J. Shu, and Q. Xu, "Suspended Si ring resonator for mid-IR application," Opt. Lett. **38**(7), 1122–1124 (2013).
13. C. Y. Wong, Z. Cheng, X. Chen, K. Xu, C. K. Y. Fung, Y. M. Chen, and H. K. Tsang, "Characterization of mid-infrared silicon-on-sapphire microring resonators with thermal tuning," IEEE Photon. J. **4**(4), 1095–1102 (2012).
14. R. Shankar, I. Bulu, and M. Lončar, "Integrated high-quality factor silicon-on-sapphire ring resonators for the mid-infrared," Appl. Phys. Lett. **102**(5), 051108 (2013).

#217370 - $15.00 USD Received 18 Jul 2014; revised 15 Aug 2014; accepted 29 Aug 2014; published 23 Sep 2014

15. A. Spott, Y. Liu, T. Baehr-Jones, R. Ilic, and M. Hochberg, "Silicon waveguides and ring resonators at 5.5.μm," Appl. Phys. Lett. **97**(21), 213501 (2010).
16. H. Lin, L. Li, Y. Zou, S. Danto, J. D. Musgraves, K. Richardson, S. Kozacik, M. Murakowski, D. Prather, P. T. Lin, V. Singh, A. Agarwal, L. C. Kimerling, and J. Hu, "Demonstration of high-Q mid-infrared chalcogenide glass-on-silicon resonators," Opt. Lett. **38**(9), 1470–1472 (2013).
17. F. Jiang, N. Duan, H. Lin, L. Li, J. Hu, L. Bi, H. Lu, X. Weng, J. Xie, and L. Deng, "ZrO_2-TiO_2 thin films and resonators for mid-infrared integrated photonics," Proc. SPIE **8988**, 89880S (2014).
18. A. Malik, M. Muneeb, Y. Shimura, J. Van Campenhout, R. Loo, and G. Roelkens, "Germanium-on-silicon mid-infrared waveguides and Mach-Zehnder interferometers," in *Proceedings of IEEE Conference on Photonics* (IEEE, 2013), pp. 104–105.
19. P. T. Lin, V. Singh, L. Kimerling, and A. M. Agarwal, "Planar silicon nitride mid-infrared devices," Appl. Phys. Lett. **102**(25), 251121 (2013).
20. V. M. N. Passaro, B. Troia, M. La Notte, and F. De Leonardis, "Photonic resonant microcavities for chemical and biochemical sensing," RSC Adv. **3**(1), 25–44 (2012).
21. W. S. Fegadolli, G. Vargas, X. Wang, F. Valini, L. A. M. Barea, J. E. B. Oliveira, N. Frateschi, A. Scherer, V. R. Almeida, and R. R. Panepucci, "Reconfigurable silicon thermo-optical ring resonator switch based on Vernier effect control," Opt. Express **20**(13), 14722–14733 (2012).
22. J. C. Hulme, J. K. Doylend, and J. E. Bowers, "Widely tunable Vernier ring laser on hybrid silicon," Opt. Express **21**(17), 19718–19722 (2013).
23. J. H. Lee, I. Shubin, J. Yao, J. Bickford, Y. Luo, S. Lin, S. S. Djordjevic, H. D. Thacker, J. E. Cunningham, K. Raj, X. Zheng, and A. V. Krishnamoorthy, "High power and widely tunable Si hybrid external-cavity laser for power efficient Si photonics WDM links," Opt. Express **22**(7), 7678–7685 (2014).
24. R. Boeck, N. A. F. Jaeger, N. Rouger, and L. Chrostowski, "Series-coupled silicon racetrack resonators and the Vernier effect: theory and measurement," Opt. Express **18**(24), 25151–25157 (2010).
25. R. Boeck, J. Flueckiger, H. Yun, L. Chrostowski, and N. A. F. Jaeger, "High performance Vernier racetrack resonators," Opt. Lett. **37**(24), 5199–5201 (2012).
26. R. Boeck, J. Flueckiger, L. Chrostowski, and N. A. F. Jaeger, "Experimental performance of DWDM quadruple Vernier racetrack resonators," Opt. Express **21**(7), 9103–9112 (2013).
27. L. Zhou, X. Zhang, L. Lu, and J. Chen, "Tunable Vernier microring optical filters with p-i-p type microheaters," IEEE Photon. J. **5**(4), 6601211 (2013).
28. R. Boeck, W. Shi, L. Chrostowski, and N. A. F. Jaeger, "FSR-eliminated Vernier racetrack resonators using grating-assisted couplers," IEEE Photon. J. **5**(5), 2202511 (2013).
29. P. B. Deotare, I. Bulu, I. W. Frank, Q. Quan, Y. Zhang, R. Ilic, and M. Loncar, "All optical reconfiguration of optomechanical filters," Nat Commun **3**, 846 (2012).
30. P. B. Deotare, L. C. Kogos, I. Bulu, and M. Loncar, "Photonic crystal nanobeam cavities for tunable filter and router applications," IEEE J. Sel. Top. Quantum Electron. **19**(2), 3600210 (2013).
31. W. S. Fegadolli, J. E. B. Oliveira, V. R. Almeida, and A. Scherer, "Compact and low power consumption tunable photonic crystal nanobeam cavity," Opt. Express **21**(3), 3861–3871 (2013).
32. P. Seidler, K. Lister, U. Drechsler, J. Hofrichter, and T. Stöferle, "Slotted photonic crystal nanobeam cavity with an ultrahigh quality factor-to-mode volume ratio," Opt. Express **21**(26), 32468–32483 (2013).
33. C.-S. Deng, H.-G. Peng, Y.-S. Gao, and J.-X. Zhong, "Ultrahigh-Q photonic crystal nanobeam cavities with H-shaped holes," Physica E **63**, 8–13 (2014).
34. M. La Notte, B. Troia, T. Muciaccia, C. E. Campanella, F. De Leonardis, and V. M. N. Passaro, "Recent advances in gas and chemical detection by Vernier effect-based photonic sensors," Sensors (Basel) **14**(3), 4831–4855 (2014).
35. L. Jin, M. Li, and J.-J. He, "Highly-sensitive silicon-on-insulator sensor based on two cascade micro-ring resonators with Vernier effect," Opt. Commun. **284**(1), 156–159 (2011).
36. D. Dai, "Highly sensitive digital optical sensor based on cascaded high-Q ring-resonators," Opt. Express **17**(26), 23817–23822 (2009).
37. J. Hu and D. Dai, "Cascaded-ring optical sensor with enhanced sensitivity by using suspended Si-nanowires," IEEE Photon. Technol. Lett. **23**(13), 842–844 (2011).
38. X. Jiang, J. Ye, J. Zou, M. Li, and J.-J. He, "Cascaded silicon-on-insulator double-ring sensors operating in high-sensitivity transverse-magnetic mode," Opt. Lett. **38**(8), 1349–1351 (2013).
39. T. Claes, W. Bogaerts, and P. Bienstman, "Vernier-cascade label-free biosensor with integrated arrayed waveguide grating for wavelength interrogation with low-cost broadband source," Opt. Lett. **36**(17), 3320–3322 (2011).
40. L. Ren, X. Wu, M. Li, X. Zhang, L. Liu, and L. Xu, "Ultrasensitive label-free coupled optofluidic ring laser sensor," Opt. Lett. **37**(18), 3873–3875 (2012).
41. M. La Notte and V. M. N. Passaro, "Ultra high sensitivity chemical photonic sensing by Mach-Zehnder interferometer enhanced Vernier-effect," Sens. Actuators B Chem. **176**, 994–1007 (2013).
42. V. Zamora, P. Lützow, M. Weiland, and D. Pergande, "Investigation of cascaded SiN microring resonators at 1.3 μm and 1.5 μm," Opt. Express **21**(23), 27550–27557 (2013).
43. X. Tu, J. Song, T.-Y. Liow, M. K. Park, J. Q. Yiying, J. S. Kee, M. Yu, and G.-Q. Lo, "Thermal independent Silicon-Nitride slot waveguide biosensor with high sensitivity," Opt. Express **20**(3), 2640–2648 (2012).
44. V. M. N. Passaro, B. Troia, and F. De Leonardis, "A generalized approach for design of photonic gas sensors based on Vernier-effect in mid-IR," Sens. Actuators B Chem. **168**, 402–420 (2012).
45. B. Troia and V. M. N. Passaro, "Investigation of a novel silicon-on-insulator rib-slot photonic sensor based on the Vernier effect and operating at 3.8 μm," J. Eur. Opt. Soc. Rapid Publ. **9**, 14005 (2014).

#217370 - $15.00 USD Received 18 Jul 2014; revised 15 Aug 2014; accepted 29 Aug 2014; published 23 Sep 2014

46. Comsol Multiphysics by COMSOL©, ver. 3.2, single license, 2005.
47. B. Troia, F. De Leonardis, and V. M. N. Passaro, "Generalized modelling for the design of guided-wave optical directional couplers," Opt. Lett. **39**(5), 1161–1164 (2014).
48. G. T. Reed, *Silicon Photonics: The State of the Art* (John Wiley, 2008), Chap. 7.

1. Introduction

In recent years, the mid-infrared wavelength range has become a very attractive and promising spectral region to be explored for a wide range of applications, such as environmental, bio-sensing, defence, security, communications, and astronomy, to name a few [1, 2]. In this context, huge research efforts have been carried out in order to extend the operation of silicon photonics from the near-infrared to the mid-infrared wavelength range. To this purpose, several results have been reported in literature on mid-infrared photonic devices, such as Mach-Zehnder interferometers (MZI), thermo optic modulators, photodetectors, multimode interference splitters, spectrometers, multiplexers and (de)multiplexers based on silicon-on-insulator (SOI) technology platform [3–10].

So far, very few results on SOI ring resonators operating in the mid-infrared have been reported. For example, a racetrack resonator based on SOI strip waveguide with the radius of 100 μm was demonstrated at wavelengths in the range 3.72-3.78 μm, exhibiting an average quality factor Q up to 8,200. Actually, as the absorption of SiO_2 is the main limitation of SOI for longer mid-infrared wavelengths, exotic SOI waveguide architectures and technology platforms have been proposed as well. For example, suspended membrane waveguide and ring resonator were demonstrated experimentally at λ = 2.75 μm with a quality factor of ~8,100 [11]. Similar devices have been demonstrated near 5.2 and 3.4 μm, revealing loaded quality factors of 2,700 and 7,900, respectively [12]. As sapphire is transparent up to 5.5 μm, microring resonators in silicon-on-sapphire (SOS) were characterized at 2.75 μm, revealing a Q-factor as high as ~11,400 [13]. Moreover, SOS ring resonators have been experimentally demonstrated at wavelengths in the range 4.3-4.6 μm [14] and 5.4-5.6 μm [15], revealing Q-factor values as high as 151,000 and 278,000 around 4 μm and 3,000 at 5.6 μm. Recently, waveguide-coupled As_2Se_3 chalcogenide glass resonators monolithically integrated on silicon have been fabricated and characterized at 5.2 μm exhibiting a very high quality factor of 2×10^5 [16]. Finally, a quality factor of 11,000 was achieved in a $Ge_{23}Sb_7S_{70}/Zr_{0.6}Ti_{0.4}O_2$ strip-loaded waveguide at 5.2 μm wavelength [17]. Although rings operating efficiently in the mid-infrared can be fabricated in several technology platforms, complementary metal-oxide semiconductor (CMOS) compatible devices would be more suitable for large-scale production and integration with Microelectronics. Nowadays, some of the most promising alternatives are represented by the germanium-on-silicon (Ge-on-Si) technology platform [18] and by the use of fully CMOS-compatible materials for planar devices, such as silicon nitride (SiN) which is transparent to 6.5 μm [19].

In this context, ring resonators are recognized as very suitable photonic devices for sensing [20] and optical signal processing (e.g., filtering, multiplexing, demultiplexing). Moreover, SOI cascade-coupled ring and racetrack resonators have been widely used to employ the Vernier effect as a very efficient solution for improving device performances. In fact, such architectures have been designed and fabricated as reconfigurable thermo-optical switches [21], as tunable lasers [22, 23] and to operate as filters suitable for advanced multiplexing and de-multiplexing in dense wavelength division multiplexing (DWDM) optical systems, revealing overall free spectral ranges (FSR) as high as 38 nm with interstitial peak suppression (IPS) of 25.5 dB [24, 25]. Furthermore, quadruple SOI Vernier racetrack resonators have been proposed for enhancing filter performance, exhibiting a FSR as large as 37.52 nm with a IPS of ~40 dB [26]. In addition, thermally tunable microring optical filters using p-i-p type microheaters have been proposed for enlarging the FSR up to ~95 nm [27] and grating assisted-couplers have been used to completely eliminate the FSR in the drop and through port of the cascaded architecture [28]. Actually, nanobeam cavities are competing devices in optical filtering applications (e.g., tunable and reconfigurable filters) since infinity FSR and Q-factor higher than 10^9 can be achieved in the near-infrared wavelength range. Moreover, spectral features of such devices can be controlled by designing cavities with

#217370 - $15.00 USD Received 18 Jul 2014; revised 15 Aug 2014; accepted 29 Aug 2014; published 23 Sep 2014

different geometries or dimensions as well as by changing the number of nanobeam cavities arranged in a one dimensional (1D) photonic crystal array [29–33].

The Vernier effect has been widely used also for the design and fabrication of ultra-high performance sensors [34–40]. In fact, experimental sensitivity as high as 24,300 nm/RIU and 2430 dB/RIU (i.e., refractive index unit) have been achieved for wavelength and intensity interrogation, respectively [38]. Moreover, a surface mass detection limit as low as 6.9 pg/mm^2 can be achieved for protein molecules [40] and a detection limit for homogeneous sensing as high as 8.3×10^{-6} RIU has also been experimentally demonstrated. The Vernier effect has been also investigated by cascading a ring resonator with a MZI [41], and by exploring different technology platforms such as SiN microring resonators [42] and MZIs based on slot waveguides revealing a surface detection limit as low as 0.155 pg/mm^2 [43].

To the best of our knowledge, the Vernier effect has not been experimentally demonstrated in the mid-infrared wavelength range. So far, very few theoretical results have been published revealing ultrahigh sensing performance at 3.39 μm [44] and 3.8 μm [45]. Since several harmful gases as well as chemical and biochemical analytes exhibit fundamental vibrational and rotational modes that are spectroscopically accessible within the mid-infrared, the interaction between mid-infrared photons and those samples provides particularly sharp transitions, which generates unique mid-infrared absorption spectra. Consequently, the fundamental advantage of operating with these high performance Vernier architectures in the mid-infrared wavelength range is the possibility of employing refractive index sensing and optical absorption sensing simultaneously, resulting in very high sensing performance. In fact, sensitivities as high as 224.4 μm/RIU and 218.51 μm/RIU have been theoretically estimated for methane and ethane detection respectively, corresponding to the detection of minimum percentages of methane and ethane in air volume equal to 2% and 1%, respectively [44].

The paper is organized as follows: SOI waveguides, bend losses and directional couplers operating in the mid-infrared are presented in Section 2. Section 3 shows the results for single racetrack resonators and cascade-coupled ones, presenting for the first time Vernier spectra in the mid-infrared. Finally, Section 4 gives the conclusions.

2. SOI platform for mid-infrared devices

All devices presented in this paper were realized by using SOI rib waveguides. The rib waveguide patterns were written using a JEOL JBX 9300FS e-beam lithography tool on 6-inch SOI wafer. A non-chemically amplified high resolution positive resist (i.e., ZEP-520A) from Nippon Zeon was used. Patterns in ZEP-520A were transferred to the SOI wafers by inductively coupled plasma (ICP) etching using an Oxford Instrument ICP 380 plasma system. The waveguides were 400 nm high, H, with 220 nm etch depth, E, and 2000 nm of buried oxide (BOX). They were fabricated with a width, W, equal to 1350 nm, resulting in single mode propagation of the fundamental quasi-TE (i.e., transverse electric) polarized optical mode. The waveguide cross section with the spatial distribution of the fundamental quasi-TE optical mode at the operating wavelength of λ = 3.75 μm, as well as the effective index, n_{eff}, of the fundamental and first order modes as a function of different rib width and etch depth values, are plotted in Figs. 1(a) and 1(b), respectively.

#217370 - $15.00 USD Received 18 Jul 2014; revised 15 Aug 2014; accepted 29 Aug 2014; published 23 Sep 2014

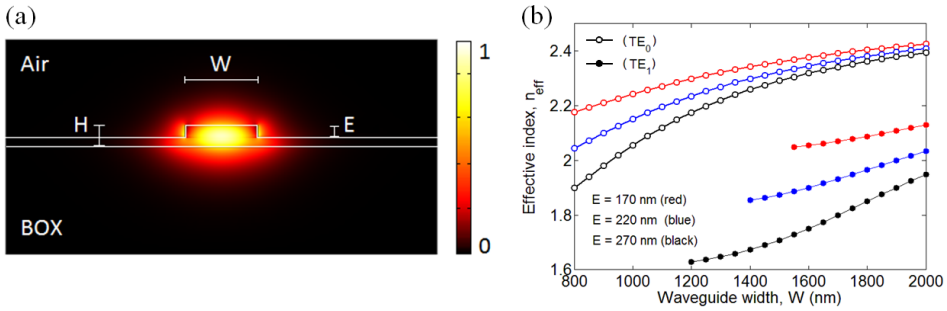

Fig. 1. (a) Spatial distribution of the fundamental quasi-TE polarized optical mode into the SOI rib waveguide (W = 1350 nm, H = 400, and E = 220 nm). (b) Effective index of the fundamental (circle) and first order (dot) modes as a function of different values of the waveguide width W and etch depth E (i.e., 170 nm, 220 nm, and 270 nm). The operating wavelength is λ = 3.75 μm.

The simulations were performed using COMSOL Multiphysics software package as well as numerical and algorithmic custom-made codes developed in the FEMLAB platform [46]. A fabrication tolerance for the waveguide width W and etch depth E of ± 20 nm was taken into account in the design procedure. Effective and group indices of the fundamental quasi-TE optical mode propagating in the rib waveguide characterized by nominal dimensions (i.e., W_{nom} = 1350 nm, E_{nom} = 220 nm) are $n_{eff,nom}$ = 2.2846 and $n_{g,nom}$ = 3.6533. In particular, both n_{eff} and n_g were calculated as a function of different values of W and E in order to investigate the influence of fabrication tolerances on the operation of directional couplers as well as single racetrack resonators and Vernier architectures. To this purpose, three-dimensional (3D) graphs of modal effective index and group index variations, Δn_{eff} and Δn_g, are plotted in Figs. 2(a) and 2(b), respectively. Both variations were calculated as the differences between nominal indices (i.e., $n_{eff,nom}$, $n_{g,nom}$) and those calculated with waveguide dimensions varied in the range ± 20 nm with respect to W_{nom} and E_{nom}.

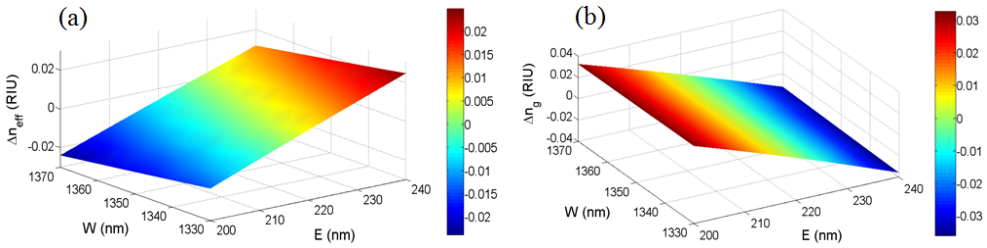

Fig. 2. (a) Δn_{eff} and (b) Δn_g as a function of fabrication tolerances at the operating wavelength of λ = 3.75 μm.

By considering $E = E_{nom}$, the maximum effective and group index variations induced by varying W in the range from W_{nom}-20 nm to W_{nom} + 20 nm, are $\Delta n_{eff,max} = 6 \times 10^{-3}$ RIU and $\Delta n_{g,max} = 6 \times 10^{-4}$ RIU. Conversely, by fixing $W = W_{nom}$ and varying E in the range E ± 20 nm, it results $\Delta n_{eff,max}$ ~2×10^{-2} RIU and $\Delta n_{g,max}$ ~3.5×10^{-2} RIU. As a result of this investigation, the etch depth (i.e., E) results to be the most critical waveguide dimension since a group index variation of the order of 10^{-2} RIU will induce wavelength shifts of racetrack resonances as large as ~35 nm, resulting in a detrimental effect particularly when two cascade micro-cavities are coupled for the generation of the Vernier effect. Furthermore, we propose in Fig. 3(b) a 3D graph of the resonance wavelength shift, $\Delta\lambda_{res}$, as a function of fabrication tolerances in case of a racetrack resonator operating in the mid-infrared. The device is based on the SOI rib waveguide previously analyzed and has an overall roundtrip length as long as L = 714 μm with a FSR of 5.4166 nm at the resonant wavelength λ_{res} = 3.7591 μm, as shown in Fig. 3(a).

#217370 - $15.00 USD Received 18 Jul 2014; revised 15 Aug 2014; accepted 29 Aug 2014; published 23 Sep 2014

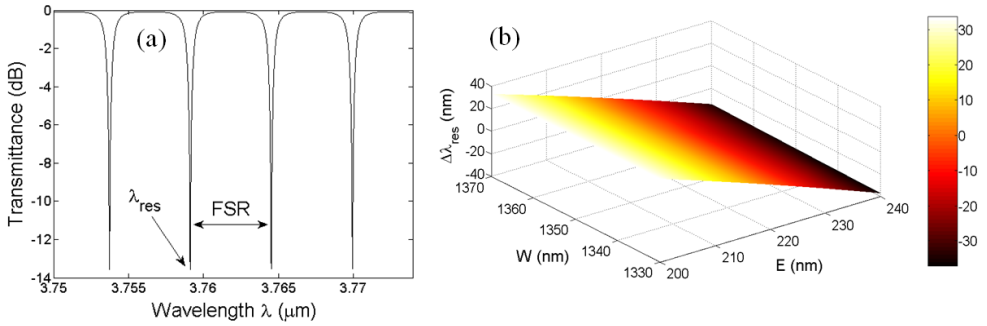

Fig. 3. (a) Mid-infrared racetrack spectrum and (b) $\Delta\lambda_{res}$ as a function of fabrication tolerances.

The 3D graph of $\Delta\lambda_{res}$ was obtained by calculating the racetrack resonance wavelength λ_{res} for the SOI rib waveguide whose width and etch depth were varied in turn, according to the fabrication tolerance mentioned previously. In particular, the 3D graph of Δn_g, as plotted in Fig. 2(b), was used to estimate λ_{res} according to the relation $\lambda_{res} = (n_g L)/m$, where m is the resonance order. As previously performed, by fixing $E = E_{nom}$, the maximum resonance wavelength shift induced by $W = W_{nom} \pm 20$ nm, is $\Delta\lambda_{res,max} = 0.633$ nm while, in case of $W = W_{nom}$ and $E = E \pm 20$ nm, it results $\Delta\lambda_{res,max} = 35.622$ nm. The parameter $\Delta\lambda_{res}$ was calculated according to the equation $\Delta\lambda_{res} = \lambda_{res}(W_{nom}, E_{nom}) - \lambda_{res}(W, E)$ and maximum values are reported without the sign. Practically, if the variation is negative a red shift of the resonance wavelength will occur otherwise a blue shift will take place, resulting in a resonance shift toward shorter wavelengths. These results confirm the etch depth as the most critical parameter for the design of single racetrack resonators as well as cascade-coupled resonators where the positions of multiple resonances assume a fundamental role in the overall device operation.

In conclusion, a fabrication tolerance of ± 10 nm for waveguide width and height should be considered as the maximum acceptable range. More precisely, the range ± 5 nm is the most suitable for the design of Vernier configurations operating in the mid-infrared and fabricated on the SOI technology platform with 400 nm-thick silicon layer on 2 μm-thick BOX layer.

2.1 Bend losses in SOI rib waveguides operating in the mid-infrared

The experimental estimation of bend losses is a fundamental step towards the design and fabrication of racetrack resonators since, to the best of our knowledge, a complete investigation has not been reported yet on this technology platform at the mid-infrared wavelength range. Few experimental results were published about bend losses in SOI strip (i.e., $W = 1000$ nm, $H = 500$ nm) and rib (i.e., $W = 2000$ nm, $E = 1200$ nm, $H = 2000$ nm) waveguides at the operating wavelength of 3.74 μm [4]. In particular, bend losses of 0.020 ± 0.002 dB/90° were measured in case of bent strip waveguides with a bend radius of $R = 100$ μm, and a loss as low as 0.01 dB/90° was obtained in bent rib waveguides with a bend radius of 200 μm.

In this paper, we report the experimental measurements of bending losses in SOI rib waveguides operating at $\lambda = 3.75$ μm and with the following dimensions: $W = 1350$ nm, $H = 407$ nm, and $E = 234$ nm. To this purpose, we designed three blocks of serpentine shaped waveguides. Each block was made of ten channels. In particular, the first one had an initial number of six 90° bends and an increasing number of twelve bends was added in each of the remaining channels in order to appreciate the separation among waveguide transmission spectra. Furthermore, we considered SOI rib waveguides with three different bend radii i.e., $R = 20$ μm, $R = 30$ μm, and $R = 40$ μm. Consequently, the total lengths of the three blocks considered for this investigation, including input and output grating couplers, were 4.56 mm, 5.7 mm, and 6.84 mm corresponding to bend radii of 20 μm, 30 μm, and 40 μm, respectively. Experimental results are plotted in Fig. 4.

#217370 - $15.00 USD Received 18 Jul 2014; revised 15 Aug 2014; accepted 29 Aug 2014; published 23 Sep 2014

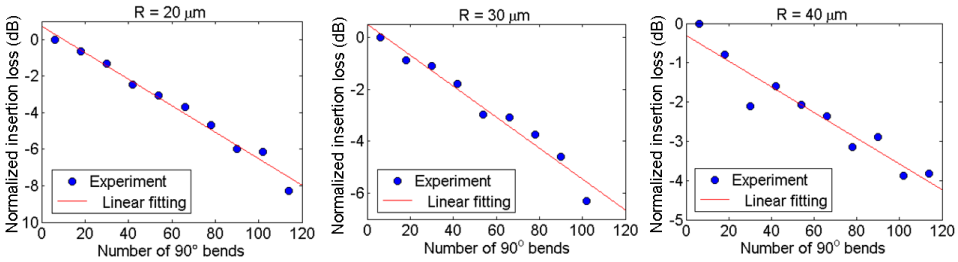

Fig. 4. Bend losses in SOI rib waveguide at λ = 3.75 μm as a function of different bend radii R.

The experimental setup described in [3] was used to characterize bent waveguides, as well as other devices presented in this paper. In particular, the light was coupled by means of grating couplers and the mid-infrared source was a tunable quantum cascade laser (QCL) emitting at 3.7-3.9 μm. In addition, a spectral sampling step size of 0.05 nm was used for the experimental data acquisitions.

Bend losses of 0.073 ± 0.003 dB/90°, 0.060 ± 0.003 dB/90°, and 0.033 ± 0.003 dB/90° were measured for the bend radii of 20 μm, 30 μm, and 40 μm, respectively. In particular, the experimental data distribution in case of R = 40 μm is the noisiest one because bend losses were low and therefore the differences between each channel transmission spectra were not as easily distinguishable as in the other two cases. These results reveal that ring and racetrack resonators as well as bent waveguides with radii even shorter than 20 μm can be designed for the fabrication of very compact SOI photonic circuits operating in the mid-infrared wavelength range of 3.7-3.8 μm, resulting in bend losses lower than 0.1 dB/90°. Finally, bending radii longer than 100 μm introduce negligible bend losses.

2.2 Directional couplers based on SOI rib waveguide in the mid-infrared

Directional couplers are crucial devices in the design of single racetrack resonators and cascade-coupled racetrack architectures. In fact, the coupling region determines the amount of optical power that is coupled from the bus waveguide to the microcavity or transferred between two coupled racetrack resonators. In this context, we implemented a sophisticated algorithmic procedure based on the general formulation of coupled mode theory (CMT) equations, as exhaustively described in [47]. In particular, the flexibility of the model allowed us to take into account several directional coupler configurations. For example, a bus waveguide coupled to a ring or racetrack resonator as well as two coupled S-bends and a straight waveguide coupled to an S-bend waveguide, to name a few. In this investigation, we considered the design and fabrication of directional couplers as shown in Fig. 5(b), in order to validate experimentally our numerical results and use the model for the accurate design of single and cascade-coupled racetrack resonators based on the Vernier effect.

In Figs. 5(a) and 5(b), L_i is the interaction length where the distance between the coupled waveguides is constant and equal to g_0, L_{tr} is the transition region length where the directional coupler gap is not constant, and D is the distance between the bus waveguides at the end of the overall coupling region. The S-bends in the top and bottom arms introduced negligible bend losses since the bend radii were almost equal to 130 μm.

Two architectures were fabricated, characterized by identical dimensions L_{tr} = 150 μm, D = 50 μm, and g_0 varied in the range from 300 nm to 750 nm in 50 nm increments. The only exception was the interaction length L_i that was set to 10 μm in one configuration and 30 μm in the other. In this way, the operation of directional couplers was different as shown in Fig. 5(a) where the power coupling coefficient κ_c^2 is plotted as a function of the directional coupler gap g_0 in case of both configurations. The comparison between numerical and experimental results reveal a very good agreement, confirming the implemented model as a useful tool for the design of Vernier architectures in which the control of the power coupling coefficients is fundamental for the correct operation of such devices.

#217370 - $15.00 USD Received 18 Jul 2014; revised 15 Aug 2014; accepted 29 Aug 2014; published 23 Sep 2014

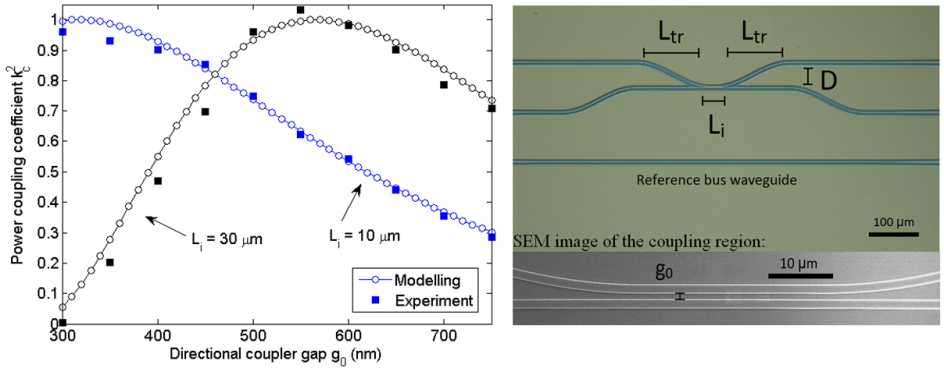

Fig. 5. (a) Experimental characterization of directional couplers in the mid-infrared. (b) Optical image of a representative device with the scanning electron microscope (SEM) image of the coupling region at the bottom.

In this context, fabrication tolerances were taken into account in the design of directional couplers as well. In Figs. 6(a) and 6(b), we show the 3D graphs of the power coupling coefficient as a function of different waveguide width and height values in the range ± 20 nm from the nominal waveguide dimensions. The maximum variations in both configurations are $\Delta\kappa_c^2 = \pm 0.1$ and the greatest deviation is caused by the etch depth variation, confirming that *E* is the most critical waveguide dimension. In addition to this, our calculations revealed that, in the case of the SOI rib waveguide considered in this investigation, the shorter the interaction length the more stable the power coupling coefficient against fabrication tolerances.

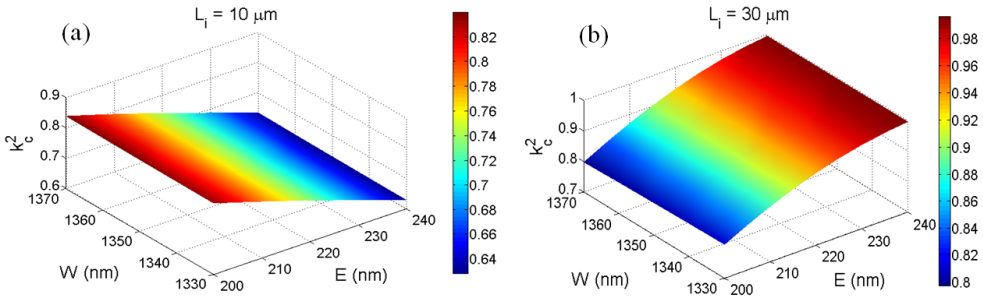

Fig. 6. Power coupling coefficient as a function of fabrication tolerances in case of similar directional couplers with g_0 = 500 nm, L_{tr} = 150 μm, D = 50 μm, (a) L_i = 10 μm, and (b) L_i = 30 μm. The operating wavelength is λ = 3.75 μm.

In conclusion, experimental results demonstrated that the optical dispersion of the SOI rib waveguide does not influence the operation of the directional couplers into the mid-infrared wavelength range from 3.7 μm to 3.8 μm. In fact, for each tested device the power coupling coefficient remained stable in the spectral range mentioned above with very small fluctuations due to the electrical noise introduced by the photodetector.

3. The Vernier effect in the mid-infrared

To the best of our knowledge, the experimental demonstration of the Vernier effect as well as the operation of SOI racetrack resonators in the wavelength range 3.7-3.8 μm, have not been reported yet. In this context, we propose the design and fabrication of two different Vernier configurations characterized by cascade-coupled racetrack resonators. To this purpose, a sophisticated algorithmic procedure based on Mason's rule and delay line signal processing

#217370 - $15.00 USD Received 18 Jul 2014; revised 15 Aug 2014; accepted 29 Aug 2014; published 23 Sep 2014

was implemented in the design [44]. The Vernier architectures labeled as Vernier #A and Vernier #B, are shown in Figs. 7(a) and 7(b).

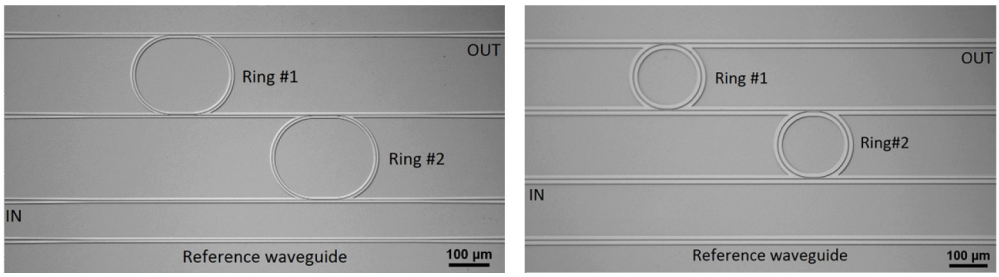

Fig. 7. Optical images of the Vernier architectures: (a) Vernier #A, (b) Vernier #B.

The Vernier effect can be achieved by cascading two coupled ring or racetrack resonators characterized by slightly different overall roundtrip lengths, L. Consequently, the resonance spectra of the two cascade-coupled resonators will exhibit different FSRs. This effect generates the unique condition in which only few resonances of both resonators will be overlapped while the other ones will be misaligned throughout the mid-infrared wavelength range. As was demonstrated in [44], the overall Vernier spectrum of such an architecture can be calculated as the product of the transmittances of both resonators (i.e., ring or racetrack), let us label them as Ring #1 and Ring #2, as shown in Figs. 7(a) and 7(b). Moreover, the overall enlarged FSR of the Vernier spectrum, $FSR_{Vernier}$, can be calculated by using Eq. (1):

$$FSR_{Vernier} = \frac{FSR_{Ring\#1} \cdot FSR_{Ring\#2}}{\left|\Delta FSR\right|} \tag{1}$$

where ΔFSR is the difference between the FSRs of Ring #1 and Ring #2.

A parameter that is usually used to estimate the performance of a Vernier architecture is the so called Vernier gain, G, defined as the ratio $FSR_{Ring\#1}/\Delta FSR$. Moreover, such architectures can operate in two different regimes, known as the first and second Vernier regimes. In particular, the second regime can be achieved when $\Delta FSR < \Delta\lambda_{FWHM(Ring\#1,\ Ring\#2)}$, $\Delta\lambda_{FWHM(Ring\#1,\ Ring\#2)}$ being the smallest full-width at half maximum (FWHM) of resonant peaks of individual racetrack resonators. On the other hand, when the above relationship is not satisfied, the Vernier architecture will work in the first operating regime. The main difference between the two Vernier regimes consists in the fact that in the first the suppression of misaligned resonances will generate two major resonance peaks separated by the spectral distance $FSR_{Vernier}$. In the second operating Vernier regime, the two peaks are separated by the same distance as before and they are constituted by several spectral lines very close to each other, resulting in a typical comb-like Vernier transmittance as shown in Figs. 8(a) and 8(b). Furthermore, the second Vernier regime is more advantageous when such architectures are designed for sensing applications. In fact, it has been demonstrated that they act practically as a single microcavity in which sensing performance is enhanced by the gain factor G (e.g., limit of detection (LOD), homogeneous and surface wavelength sensitivity) [44].

The design of Vernier architectures can be quite challenging because the position of racetrack resonances dramatically depends on fabrication tolerances as demonstrated in Fig. 3. In addition, the relationship to be satisfied in order to select between the first or second operating regime, requires a very accurate *a priori* estimation of power coupling coefficients as well as of propagation roundtrip losses into the SOI racetrack resonators. Moreover, the material dispersion was taken into account in the design since it can influence the operation of such devices because of resonant wavelength shifts and power coupling coefficient changes induced by waveguide effective index variations as a function of the operating wavelength. Finally, each Vernier architecture is characterized by four directional couplers that allow

#217370 - $15.00 USD Received 18 Jul 2014; revised 15 Aug 2014; accepted 29 Aug 2014; published 23 Sep 2014

guiding of the optical signal from the input channel to the output one, as indicated in Figs. 7(a) and 7(b).

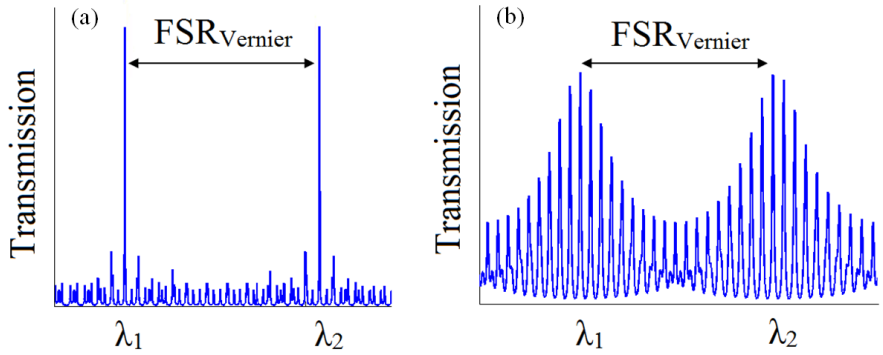

Fig. 8. Qualitative transmission spectra of Vernier architectures operating in the (a) first and (b) second regimes.

A detailed theoretical investigation on general criteria to be chosen for the design of Vernier devices operating in the mid-infrared was presented in [44]. In particular, each racetrack resonator is characterized by symmetrical directional couplers. The coupling regions were properly designed in order to make the power coupling coefficients as equal as possible shaping resonance peaks of racetrack resonator spectra to allow the operation of such devices in the second operating Vernier regime.

Geometrical and optical experimental parameters of well-performing racetrack resonators designed for Vernier architectures, are listed in Table 1.

Table 1. Optical and geometrical experimental parameters of racetrack resonators operating in the mid-infrared

Parameters	Vernier #A		Vernier #B	
Racetrack label	Ring #1	Ring #2	Ring #1	Ring #2
FSR (nm)	5.33	5.06	13.94	13.20
L (μm)	714	753.5	274	284
R (μm)	98	104	42	43
L_i (μm)	49.2	50	5	7
g_0 (nm)	900	900	300	300
κ_c^2	0.70	0.72	0.69	0.79
IL_{avg} (dB)	1.77	1.33	1.48	3.1
ER_{max} (dB)	25	29	25	30
Q-factor	~2,900	~2,500	~940	~850
$\Delta\lambda_{FWHM}$ (nm)	1.9	1.5	3.8	4.4

Spectra of single racetrack resonators whose parameters are listed in Table 1, are plotted in Fig. 9. A minimum average insertion loss (IL_{avg}) of 1.33 dB and a maximum extinction ratio (ER_{max}) of 30 dB were achieved. The group index was estimated experimentally by fitting Eq. (2) [48] and its value, very close to 4, revealed a good agreement with theoretical results.

$$FSR = \frac{\lambda_{res}^2}{(2\pi R + 2L_i)n_g} \tag{2}$$

Furthermore, a good agreement was also achieved between experimental and numerical spectra, revealing the accuracy as well as the efficiency of the theoretical modelling and fabrication facilities employed in this investigation.

#217370 - $15.00 USD Received 18 Jul 2014; revised 15 Aug 2014; accepted 29 Aug 2014; published 23 Sep 2014

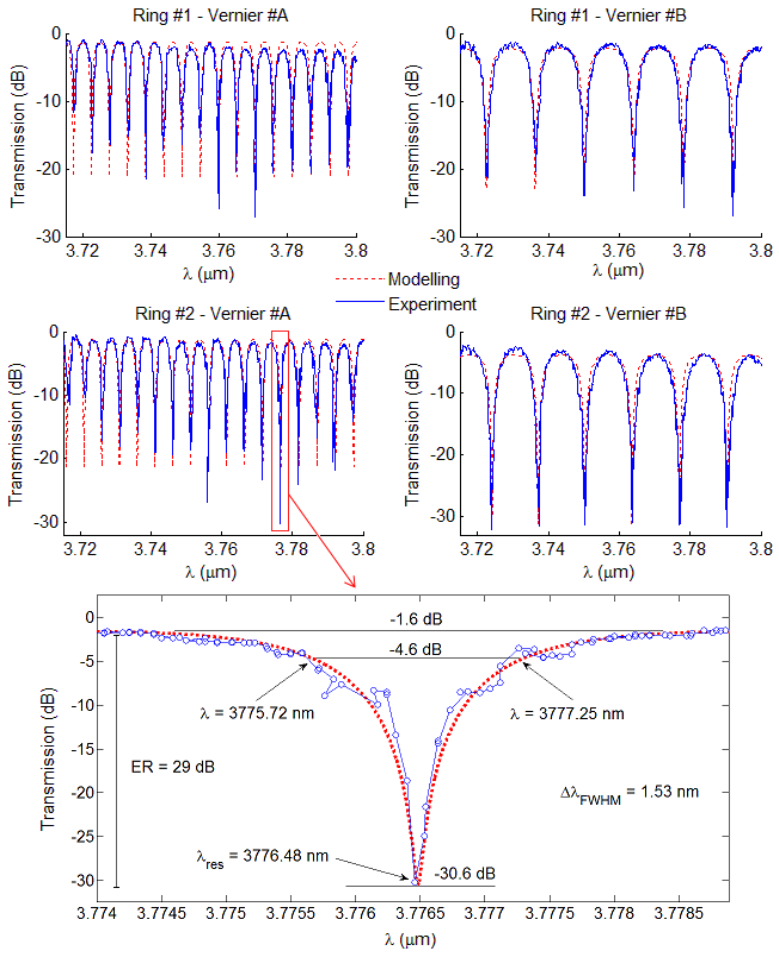

Fig. 9. Normalized spectra of racetrack resonators (i.e., Ring #1, Ring #2) of each Vernier architecture, Vernier #A and Vernier #B. A Q-factor of ~2.5×10^3 with an extinction ratio of 29 dB can be seen at the bottom.

It is worth noting that because of the mode-hopping behavior of the commercial laser employed for these measurements, it is difficult to interrogate fine wavelength features, and this is the reason why some resonance peaks were clipped. Actually, the experimental setup imposed the design of racetrack resonators with FSR larger than 5 nm otherwise it could have been difficult to detect the shape of very close and deep resonances. In addition, loaded Q-factors measured experimentally and listed in Table 1 are quite low if compared, for example, with those achieved by ring resonators operating in the mid-infrared and fabricated on SOS technology platform [13–15]. Actually, we measured Q-factors higher than 10,000 in racetrack resonators fabricated with different values of the directional coupler gap g_0 and these racetrack resonators were demonstrated to be suitable for the Vernier effect in the second operating regime. However, the spectra of such single resonators were affected by clipped resonances making the detection of the overall Vernier spectra quite challenging sometimes.

By cascading racetrack resonators Ring #1 and Ring #2, we demonstrated the Vernier effect in the 3.7-3.8 μm wavelength range. In particular, the best Vernier spectra were measured in Vernier architectures Vernier #A and Vernier #B with directional coupler gaps equal to g_0 = 510 nm and g_0 = 500 nm, respectively. The overall Vernier spectra are plotted in Fig. 10 and they were measured by interrogating both architectures at the input and output

#217370 - $15.00 USD Received 18 Jul 2014; revised 15 Aug 2014; accepted 29 Aug 2014; published 23 Sep 2014

ports as indicated in Figs. 7(a) and 7(b). Finally, optical and geometrical experimental parameters of cascade-coupled racetrack resonators are listed in Table 2.

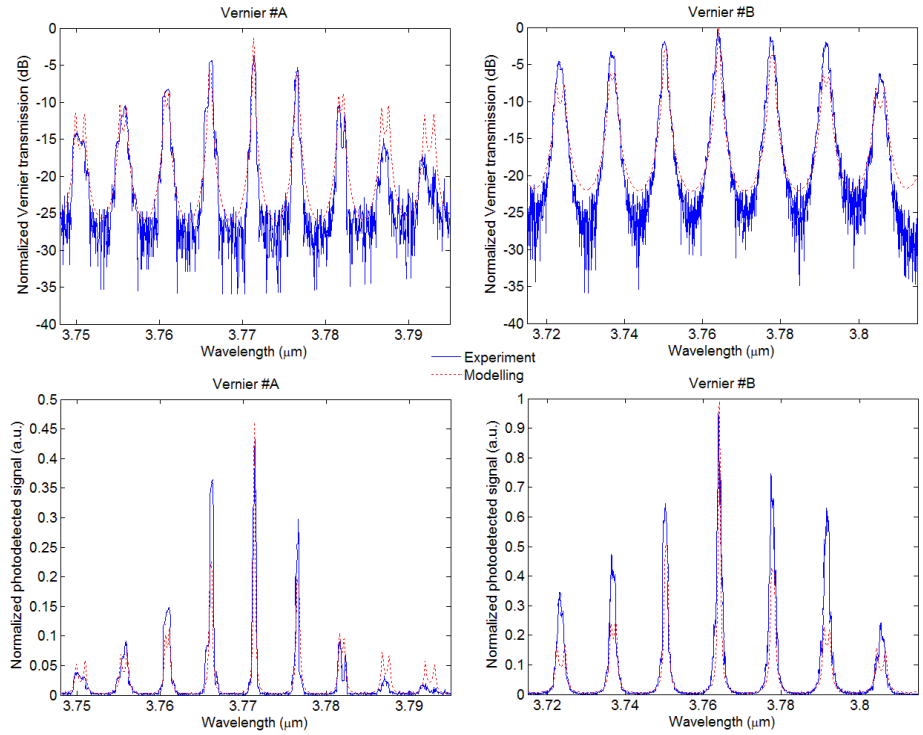

Fig. 10. Mid-infrared spectra of Vernier architectures Vernier #A and Vernier #B.

The second operative regime was achieved in both devices, according to experimental values of $\Delta\lambda_{FWHM}$ listed in Table 2. The overall Vernier peak was made by interstitial resonances with descending transmission peaks distributed symmetrically around the fundamental one centered at the wavelength in which the resonances of cascade-coupled racetrack resonators were totally overlapped. Furthermore, the matching with the theoretical model was accurate with only the exception of some spectral spikes that were probably too thin to be detected by the QCL source.

Table 2. Optical and geometrical experimental parameters of cascade-coupled racetrack resonators operating in the mid-infrared

Parameters	Vernier #A		Vernier #B	
Racetrack label	Ring #1	Ring #2	Ring #1	Ring #2
FSR (nm)	5.33	5.06	13.94	13.20
L (μm)	714	753.5	274	284
R (μm)	98	104	42	43
L_i (μm)	49.20	50	5	7
g_0 (nm)	510	510	500	500
κ_c^2	0.42	0.37	0.32	0.38
IL_{avg} (dB)	< 1	< 1	< 1	< 1
ER_{max} (dB)	15.5	10.7	22	27.8
Q-factor	~9,000	~9,400	~2,250	~1,630
$\Delta\lambda_{FWHM}$ (nm)	0.42	0.40	1.67	2.30

Over the entire wavelength range shown in Fig. 10, the configurations labeled as Vernier #A and Vernier #B exhibited a maximum peak suppression almost equal to 10 dB and 5 dB, respectively. The IPS (i.e., the difference between a major peak and the highest interstitial peak) was measured as ~2 dB and ~3.7 dB for the configurations Vernier #A and Vernier #B,

#217370 - $15.00 USD Received 18 Jul 2014; revised 15 Aug 2014; accepted 29 Aug 2014; published 23 Sep 2014

respectively. In addition, optical parameters such as IL, ER, the Q-factors measured at the central Vernier peak, the distance between adjacent resonances $\Delta\lambda_{Vernier}$, the $FSR_{Vernier}$, the FSR difference ΔFSR, and the Vernier gain G, are listed in Table 3.

Table 3. Optical experimental parameters of Vernier architectures operating in the mid-infrared

Optical parameters	Vernier #A	Vernier #B
IL (dB)	3.6	< 1
ER (dB)	25	25
Q-factor	8,000	3,200
$\Delta\lambda_{Vernier}$ (nm)	~5.5	~14
ΔFSR (nm)	0.27	0.74
$FSR_{Vernier}$ (nm)	98	249
G	19.40	18.87

The experimental demonstration of the Vernier effect in two different configurations validated the accuracy and reliability of our design procedure. In addition, estimated theoretical sensing performance revealed an homogeneous wavelength sensitivity, S_λ, of ~10^3 nm/RIU and a LOD of about 10^{-3} RIU. These results were calculated with respect to the SOI rib waveguide homogenous sensitivity S_h = 0.095. Consequently, better results can be achieved by employing more sensitive photonic waveguides such as slot waveguides with sensitivity almost equal to one and by optimizing the design of these architectures for sensing purposes [44]. In addition, it is worth noting that a low IPS is not a detrimental effect if such architectures are designed as integrated photonic spectrometers since a comb-like spectrum is suitable for finding out the fingerprint of the gas or chemical analyte characterized by vibrational modes in the mid-infrared. However, even if IL and ER are good enough to demonstrate the efficiency of such Vernier architectures for photonic signal processing and sensing applications in the mid-infrared, further improvements can be achieved. For example, $\Delta\lambda_{Vernier}$ (i.e., the maximum FSR between $FSR_{Ring\#1}$ and $FSR_{Ring\#2}$) can be reduced by designing longer racetrack resonators as it has been demonstrated in this paper. Moreover, the overall Vernier gain G can be increased by fabricating racetrack resonators with very small values of ΔFSR (e.g., ~pm). Finally, the IPS, which mainly depends on power coupling coefficients, can be enhanced by designing Vernier architectures with low power coupling coefficients (i.e., < 0.2) and operating in the first Vernier regime that is the most advantageous if the device operates as an optical filter.

4. Conclusions

In this paper, to the best of our knowledge, the first demonstration of the Vernier effect in the mid-infrared wavelength range 3.7-3.8 μm, has been presented. In particular, IL lower than 1 dB, ER of 25 dB and IPS up to 3.7 dB have been demonstrated with two different Vernier configurations. Racetrack resonators based on SOI rib waveguides have been presented as well, revealing IL lower than 1 dB and ER up to 30 dB.

Experimental results on bend losses in SOI rib waveguides have been reported as a function of different bend radii. In particular, the highest bending loss of 0.073 ± 0.003 dB/90° has been measured in case of R = 20 μm. Moreover, the experimental characterization of directional couplers in the mid-infrared wavelength range has been demonstrated, revealing a good agreement with simulations.

A detailed investigation of fabrication tolerances has been also presented, focusing on the main design guidelines to be followed for further design of such architectures operating in the mid-infrared and representing an interesting platform for innovative photonic sensors and spectrometers.

#217370 - $15.00 USD Received 18 Jul 2014; revised 15 Aug 2014; accepted 29 Aug 2014; published 23 Sep 2014

Acknowledgments

G. Z. Mashanovich would like to acknowledge support from the Royal Society through his University Research fellowship. This work was funded in part by the EPSRC project MIGRATION (EP/L01162X/1) and in part by the FP7 project MERMIG (grant n. 313037).

#217370 - $15.00 USD Received 18 Jul 2014; revised 15 Aug 2014; accepted 29 Aug 2014; published 23 Sep 2014